Vortex-ring-induced internal mixing upon the coalescence of initially stationary droplets

Xi Xia, Chengming He, Dehai Yu, Jiaquan Zhao, and Peng Zhang[*]
Department of Mechanical Engineering, The Hong Kong Polytechnic University, Hong Kong, China

This study numerically investigates the internal jetlike mixing upon the coalescence of two initially stationary droplets of unequal sizes by employing the volume of fluid method with an adaptive mesh refinement algorithm. The emergence of the internal jet is attributed to the formation of a main vortex ring, as the jetlike structure shows a strong correlation with the main vortex ring inside the merged droplet. By tracking the evolution of the main vortex ring together with its circulation, we identified two mechanisms that are essential to the internal-jet formation: the vortex-ring growth and the vortex-ring detachment. Recognizing that the initiation of the vortex-ring-induced jet energetically relies on the merged interface but the manifestation of the jet physically relies on the competition between the convection and viscous dissipation of the vortex ring, we further developed and substantiated a vortex-ring-based Reynolds number ($\mathrm{Re}_J = \Gamma_{\mathrm{VD}}/4\pi\nu$) criterion, where Γ_{VD} is the circulation of the detached main vortex ring and ν is the liquid kinematic viscosity, to interpret the occurrence of the internal jet at various Ohnesorge numbers and size ratios. For the merged droplet with apparent jet formation, the average mixing rate after jet formation increases monotonically with Re_J, which therefore serves as an approximate measure of the jet strength. In this respect, stronger internal jet is responsible for enhanced mixing of the merged droplet.

I. INTRODUCTION

Droplet coalescence is a frequent event in many natural and industrial processes involving dispersed two-phase system of either gas–liquid or liquid–liquid [1–4]. A prominent example is the dense spray of liquid fuel in the combustor of a diesel [5,6], gas turbine [7], or rocket engine [8–10]. The large concentration of droplets in the spray along with the flow nonuniformity in the combustor imply frequent droplet collisions. Among various outcomes of droplet collision, droplet coalescence is of paramount importance because it affects the concentration and size distribution of colliding droplets, and in turn the subsequent spray and combustion characteristics [11]. Droplet coalescence is also an arguably important mechanism for explaining the size distribution of droplets in rain clouds [12,13].

Early relevant studies were focused on quantifying the different regimes, namely coalescence, bouncing, and separation, that could emerge for two colliding droplets. Two governing parameters for the collision of two equal-size droplets were identified to be the Weber number, We, which measures the relative importance of droplet inertia compared to the surface tension, and the impact parameter, B, which measures the deviation of droplet trajectory from the head-on collision ($B = 0$) [14–20]. Other than We and B, the ambient gas pressure [21–23] and the size difference of the droplets [14,17,24–26] were also found to significantly influence the outcome of droplet collision. Despite of the complications at medium-to-large We, all these studies confirmed that the droplets would always coalesce for sufficiently small We. To this end, We $= 0$ guarantees the eventual merging of two droplets in any situation and has been a default setup for studying droplet coalescence.

Among previous droplet coalescence studies, a majority of the effort has been dedicated to the theoretical, experimental, and numerical investigations [27–33] of the evolution of the neck or

---

[*]pengzhang.zhang@polyu.edu.hk

bridge between two merging droplets. Similar problems have been extensively studied by other researchers such as the merging of cylinders in the Stokes flow regime modeled by Hopper [34,35], the sintering of cylinders and spheres simulated by van de Vorst [36,37], and the droplet coalescence on surfaces by Narhe *et al.* [38], Ristenpart *et al.* [39], Boreyko and Chen [40], Lee *et al.* [41], and Liu *et al.* [42]. However, less attention was focused on the outcome of the merging process, for example, the internal mixing within the coalesced droplet, which is crucial to applications involving biological or chemical reactions [43,44]. Because the internal mixing after coalescence is minimal for two identical droplets due to the intrinsic symmetry, it can be enhanced only by breaking the symmetry. Blanchette [45] numerically investigated the internal mixing within the coalesced droplet with varying surface tension and found that the surface tension variation results in faster mixing than the geometric effect. Anilkumar *et al.* [46] experimentally observed a jetlike mixing after the coalescence of two initially stationary water–glycerin solution droplets of unequal sizes. For the highly viscous droplets, noticeable mixing was however not observed in their experiments, and instead, the smaller droplet simply lodges onto the larger droplet after coalescence.

To understand the internal mixing associated with the jetlike structure, Nobari and Tryggvason [47] employed the front-tracking method to simulate the coalescence of two stationary droplets. Their results suggest that the penetration depth of the fluid from the small drop monotonically changes with the size ratio in a very viscous drop where no internal jet forms, and that this monotonicity however does not hold for small viscosity drops where internal jet could appear. Later, Liu *et al.* [48] simulated the mixing of unequal-size droplets with emphasis on elucidating the important role of the surface energy of the merged interface in forming the jetlike mixing. They found that increasing the droplet viscosity suppresses the mixing and increasing the size disparity promotes the mixing. Recently, Tang *et al.* [10] experimentally investigated the coalescence of two unequal-sized droplets with nonzero Weber numbers and observed the nonmonotonic emergence of the jetlike mixing with increasing We. Specifically, the jetlike mixing emerged at small We, in accordance with previous observations for initially stationary droplet coalescence [46,47], but such a mixing was absent at higher We as the increased droplet deformation absorbed the impact energy and therefore suppressed the jet formation. As We further increases, the jetlike mixing reemerges while it shows a "two-leg" configuration. The jetlike internal mixing was also reported in several other numerical studies employing the volume of fluid (VOF) method [49] and the lattice Boltzmann method [50–52]. Nevertheless, physical interpretation of the internal jet and its effect on mixing have not been adequately addressed in these studies.

Similar internal-mixing phenomenon has also been observed in the coalescence of a droplet into a liquid pool [53–55]. A mechanism based on the generation of vorticity by accelerated flows at curved liquid-free surfaces was proposed to explain the formation of the vortex ring [53,55–57]. Specifically, in a homogeneous fluid without body force (or with conservative body force), which is the fluid in either the droplets or the ambient gas, the rate of change of vorticity, $\boldsymbol{\omega}$, associated with a fluid element is given by the vorticity transport equation (also known as the Helmholtz vorticity equation) [58],

$$\frac{D\boldsymbol{\omega}}{Dt} = \boldsymbol{\omega} \cdot \nabla \boldsymbol{u} + \nu \nabla^2 \boldsymbol{\omega}, \tag{1}$$

where $\boldsymbol{u}$ is the velocity and ν is the kinematic viscosity. The first term on the right-hand side of Eq. (1) represents the stretching and tilting effect of the vortex-line, which is balanced by the change of vortex strength caused by the changes in the area and direction of the fluid element surface (pp. 268–269 of Ref. [58]); the second term is the vorticity diffusion term, which by nature only causes the redistribution of vorticity in the presence of vorticity gradient. Equation (1) mathematically dictates that vorticity is only a transport quantity, meaning no vorticity can be created inside a homogeneous fluid. This interpretation, although elucidated by Batchelor [58] and Cresswell and Morton [53], has not been sufficiently recognized probably because of its non-intuitive differential form. Similar conclusion can also be deduced from an integral form of Eq. (1), known as the Kelvin's circulation theorem [59,60] (or equivalently the Helmholtz's theorems [60]). Although the Kelvin's circulation theorem was originally derived for inviscid flows,

Batchelor [58] extended it to viscous flows by deriving the total change of the circulation (Γ) around an arbitrary material contour in the form (Eq. (5.2.7) of Ref. [58]),

$$\frac{d\Gamma}{dt} = -\nu \oint (\nabla \times \boldsymbol{\omega})d\boldsymbol{l}, \tag{2}$$

where $d\boldsymbol{l}$ is a material line element along the integration contour. Equation (2) can be viewed as the equivalent form of the Kelvin's circulation theorem for viscous flows. It clearly indicates that the vortex strength of any material volume does not change unless vorticity diffusion happens at the boundary by means of viscosity. Since diffusion is a transport phenomenon which does not introduce new quantity into the global system, vorticity must be generated at the boundaries where the homogeneous condition breaks or special boundary condition is in force. For inertialess drop coalescence with no initial vorticity and in the absence of rigid boundaries, the only source of vorticity must be the liquid–gas interface [53]. As the liquid–gas interface can be approximated by a free surface of a viscous fluid, the vanishing shear stress requires a nonzero jump in velocity gradients and therefore generates a finite vorticity [53,55]. The vortex ring formation after coalescence is a synergic consequence of the vorticity generation on the liquid-gas interface, the vorticity transport (including accumulation and advection) to the droplet interior, and the vorticity diffusion within the droplet. To the knowledge of the authors, no attempts have been made to describe such a vorticity evolution for binary droplet coalescence.

In the present study, we aim to numerically investigate the coalescence of initially stationary droplets of unequal sizes. The first focus of the study is the jetlike internal mixing upon the droplet coalescence and its parametric dependence on liquid viscosity, surface tension and size differential. The second is to analyze the evolution of concomitant vorticity and its interrelation with the internal mixing. Regardless of the fact that droplet collision with increasing We may enhance the internal mixing, only initially stationary droplets (i.e., with a zero Weber number) was considered in the study based on the following considerations. First, the coalescence of initially stationary droplets can be treated as a leading order approximation to that with small We. More importantly, the coalescence of initially stationary droplets occurs at the contact point of two spherical droplets, which do not deform prior to coalescence [61]. At nonzero We, the complicated phenomena of draining the intervening gas film out of the gap between two colliding droplets [61] and the succeeding interface merging at the length scales of the van der Waals force pose great challenges to numerical simulation. The additional difficulty of dealing with droplet coalescence at nonzero Weber numbers will be avoided in the present study although it merits future studies.

The structure of the paper is organized as follows: the description of the problem, the specifications of numerical methods, and the analysis of grid independence are presented in Sec. II, followed by the comparison with the available experimental results in the literature, in Sec. III. The phenomenological description of the jetlike mixing for three representative liquids such as water, *n*-decane and *n*-tetradecane are discussed in Sec. IV. An analysis of vorticity evolution is presented in Sec. V to substantiate that the internal jet formation correlates with the vortex ring generated after droplet coalescence. The essential mechanism for internal jet formation is further elucidated through the quantitative analysis of the vorticity generation at the gas–liquid interface, and the subsequent formation, growth, and detachment of the main vortex ring. In Sec. VI, a vortex-ring-based Reynolds number, characterizing the strength of the detached main vortex ring relative to the viscosity, is proposed as the criterion for the internal jet formation. Finally, the internal mixing is quantified in Sec. VII by using a mixing index, and the resultant mixing rates are compared among different cases to demonstrate the crucial impact of the internal jet on the mixing performance of the merged droplet.

II. NUMERICAL SPECIFICATIONS

We consider two initially stationary droplets, which are made to coalesce with each other at the point of contact at time $t = 0$, as illustrated in Fig. 1. A cylindrical coordinate is established so that the line connecting the mass centers of the two spherical droplets forms the axial (z-) direction.
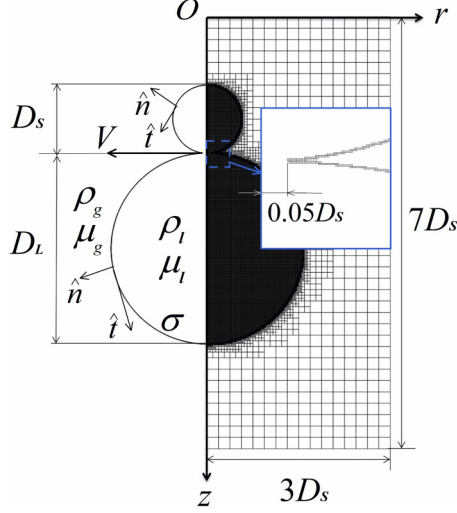
FIG. 1. Computational domain and adaptive mesh for the current droplet coalescence study. The symmetry boundary condition is specified on the axis of symmetry and free outflow boundary conditions are specified on the other three boundaries. The zoomed-in window shows the grid configuration of the interface at the initial time of contact.

The diameters of the smaller and the larger droplets are D_S and D_L, respectively. The flows in both gas and liquid droplets are viscous and incompressible. The density and viscosity are ρ_l and μ_l for the liquid, and ρ_g and μ_g for the gas, respectively. The surface tension coefficient of the gas–liquid surface is σ. The tangential and normal directions in a local coordinate system established on the droplet interface are denoted by $\hat{t}$ and $\hat{n}$, respectively.

Under the conditions that concern the present study, the gas–liquid density ratio ρ_g/ρ_l is of $O(10^{-3})$ and gas–liquid viscosity ratio μ_g/μ_l is of $O(10^{-2})$, so that they are assumed to have insignificant influence on the problem, as substantiated in the previous studies. Consequently, only two controlling non-dimensional parameters are considered, namely, the Ohnesorge number, which is defined as $\mathrm{Oh} = \mu_l/\sqrt{\rho_l \sigma D_S}$ and measures the relative importance of viscous stress and surface tension, and the size ratio, defined as $\Delta = D_L/D_S$. In the present study, the Ohnesorge numbers are in the range of $8.3 \times 10^{-3} \sim 3.6 \times 10^{-2}$ and the size ratios varies from 1.0 to 3.2, which are similar to those considered in the experiments of Zhang *et al.* [62]. The characteristic length, time and velocity, D_S, $t_c = \sqrt{\rho_l D_S^3/\sigma}$ and $v_c = \sqrt{\sigma/\rho_l D_S}$, are used to nondimensionalize the present mathematical formulations. It is noted that t_c is slightly larger than the natural oscillation time of the smaller droplet, $(\pi/4)\sqrt{\rho_l D_S^3/\sigma}$. Based on these characteristic physical quantities, the Reynolds number can be defined as $\mathrm{Re} = \sqrt{\rho_l \sigma D_S}/\mu_l$, which is the reciprocal of Oh. Thus, Re is of the order between $O(10^1)$ and $O(10^2)$, indicating that the droplet coalescence cases of the current study belong to the inertial-dominant and the inertial-viscous regimes.

The present numerical simulation adopts the volume of fluid (VOF) method [63,64], which has been implemented in the open source code, Gerris [65,66], and widely used in many multiphase flow problems [33,54,67,68]. To briefly summarize the method, the continuity equation and the incompressible Navier-Stokes equation expressed as

$$\partial \rho/\partial t + \boldsymbol{\nabla} \cdot (\rho \boldsymbol{u}) = 0, \tag{3}$$

$$\rho(\partial \boldsymbol{u}/\partial t + \boldsymbol{u} \cdot \boldsymbol{\nabla} \boldsymbol{u}) = -\boldsymbol{\nabla} p + \boldsymbol{\nabla} \cdot (2\mu \boldsymbol{D}) + \sigma \kappa \delta_s \boldsymbol{n}, \tag{4}$$
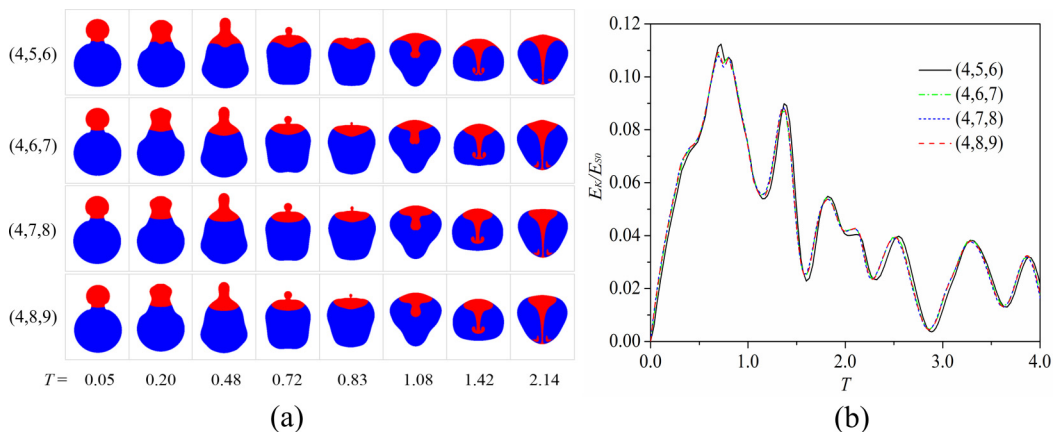
FIG. 2. Grid independence study for the simulation. (a) Comparison of droplet deformation and internal mixing pattern among different mesh levels, (4, 5, 6), (4, 6, 7), (4, 7, 8), and (4, 8, 9), where the three numbers in parenthesis are the mesh levels for the gas zone, the fluid zone, and the interface zone, respectively; (b) Comparison of the total kinetic energy, E_K, normalized by the initial surface energy, E_{S0}, for the different meshes presented in (a).

are solved using the classic fractional-step projection method. Here, $\boldsymbol{u}$ is the velocity vector, ρ is the density, μ is the dynamic viscosity, and $\boldsymbol{D}$ is the deformation tensor defined as $D_{ij} = (\partial_i u_j + \partial_j u_i)/2$. The last term on the right-hand side of Eq. (4) is the Laplace-pressure formula for the surface tension, where κ is the curvature and $\boldsymbol{n}$ is the unit normal vector of any surface, with the representation of the Dirac delta function δ_s distributing the force among the interface cells. The volume-of-fluid function describing the fluid phase is solved by the advection scheme,

$$\partial c/\partial t + \boldsymbol{\nabla} \cdot (c\boldsymbol{u}) = 0, \tag{5}$$

where c is the volume fraction, with $c = 1$ denoting droplet phase, $c = 0$ the gas phase, and $0 < c < 1$ the gas–liquid interface. Thus, the density and the viscosity of each fluid element are constructed as $\rho(c) = c\rho_l + (1 - c)\rho_g$ and $\mu(c) = c\mu_l + (1 - c)\mu_g$, respectively. For the present problem that is intrinsic axisymmetric, the axisymmetric boundary condition ($\partial/\partial r = 0$) is enforced at the z axis. At all the other boundaries, the flow is assumed to approach the condition in the far field, so the outflow boundary condition ($\partial \boldsymbol{u}/\partial n = 0$, $p = 0$) is specified.

The VOF method is characterized by the combination of the adaptive quad/octree spatial discretization, the geometrical VOF interface reconstruction, the continuum-surface-force surface tension formulation, and the height-function curvature estimation. In order to resolve the droplet interface and the internal flow within the droplet, the computational domain is divided into three zones, namely the gas, the droplet interior and the interface. The mesh for each zone can be adaptively refined to a prescribed level, denoted by an integer N, at which the minimum cell size in the zone is of $O(2^{-N})$ of the zone dimension. Accordingly, we can use (N_1, N_2, N_3) to describe the refinement levels in all the three zones. As an example, Fig. 1 shows an initial mesh at the refinement levels (5, 6, 7), in which the number of grid points is 13 851, equivalent to about 50 000 grid points in a uniform mesh system. The computational domain is an axisymmetric cylinder of $7D_S$ in length and $3D_S$ in radius. Further extension of the domain has negligible influence on the results.

The grid independence of the computational results was examined in Fig. 2. Figure 2(a) shows the comparison of droplet deformation and internal mixing pattern for the coalescence of water droplets with Oh = 8.28×10^{-3} and $\Delta = 2.0$. Four different mesh refinement levels, (4, 5, 6), (4, 6, 7), (4, 7, 8), and (4, 8, 9), were employed, which correspond to 5 351, 12 878, 40 180, and 142 897 grid points, respectively. The maximal grid points on equivalent uniform meshes are 86 016, 344 064, 1 376 256, 5 505 024, respectively. It is seen that all results in Fig. 2(a) are qualitatively similar to
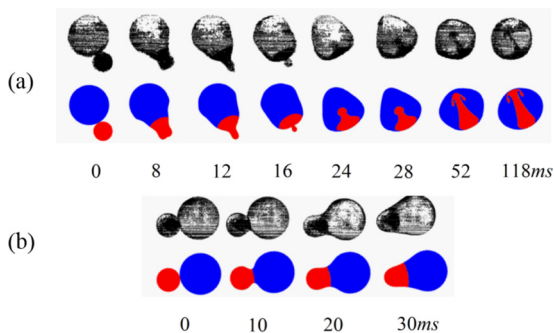
FIG. 3. Comparison of the droplet mixing patterns between experiment [46] and simulation. (a) Jet forming for a mixture of silicone oil and bromobenzene (3.3 CP measured viscosity), We = 0.0, Oh = 0.012, $\Delta = 2.08$, $t_c = 20.2$ ms, (b) no jet for a high viscous silicone oil (99.0 CP measured viscosity), We = 0.0, Oh = 0.203, $\Delta = 1.75$, $t_c = 57.5$ ms.

each other, although the mesh (4, 5, 6) seems to render a slightly different internal jet pattern than the rest three finer meshes. For quantitative justification, Fig. 2(b) further compares the evolution of the total kinetic energy (E_K) of the droplet, normalized by its initial surface energy (E_{S0}), for the same four meshes. The results are consistent with Fig. 2(a) that the latter three meshes tend to share an identical curve, which slightly deviates from the first mesh (4, 5, 6). The above discussions suggest that the mesh (4, 6, 7) is sufficient for the current study. For a balance between accuracy and computational cost, the refinement level (4, 6, 8) were used in all the following computations. A typical simulation run up to $T = 4.0$ takes approximately five hours of real time on two Intel Xeon E5-2630 processors with 12 cores.

The initial condition of the simulation setup is illustrated in the zoomed-in plot of Fig. 1. Because the interface constructed by the VOF method intrinsically has a finite thickness, the initial merging between the front surfaces of two drops inevitably causes a finite radius of the neck region as shown in the figure. This initial neck can be slightly adjusted by changing the local grid resolution around the initial contact point. To study the impact of the initial neck, three different initial radii, $0.035D_S$, $0.048D_S$, and $0.060D_S$, are simulated. Similar analysis to the grid independence study were performed, and no notable difference was observed among the different cases. The results are not presented here because they are almost identical to Fig. 2. Thus, the initial neck radius has negligible effect on the long-term process of drop coalescence. In practice, the initial neck radius of $0.048D_S$ was applied for all the following simulations.

III. EXPERIMENTAL VALIDATIONS

To validate the present numerical methods, the coalescence of two initially stationary droplets made of a mixture of silicon oil and bromobenzene in the environment of water was first simulated and compared with the experiment of Anilkumar et al. [46], as shown in Fig. 3(a). The corresponding nondimensional parameters are Oh = 0.012, $\Delta = 2.08$, $\rho_g/\rho_l = 10^{-3}$, and $\mu_g/\mu_l = 0.03$. It is seen that the simulation results are in good agreement with the experimental images in terms of the evolution of droplet deformation and that of the jetlike internal mixing. Anilkumar et al.'s experiment on the coalescence of two initially stationary droplets of silicone oil in water, corresponding to Oh = 0.203, $\Delta = 1.75$, $\rho_g/\rho_l = 1.27 \times 10^{-3}$, and $\mu_g/\mu_l = 10^{-3}$, shows that the jetlike mixing is absent because of the significantly increased droplet viscosity, as seen in Fig. 3(b). The simulation results also reproduce the experimental observation in that the smaller droplet lodges on the larger one to form a dome shape.

Figure 4 compares the present simulation with Thoroddsen et al.'s experiment [29] of water droplet coalescence in atmospheric air with Oh = 2.5×10^{-3}, $\Delta = 1.06$, $\rho_g/\rho_l = 1.23 \times 10^{-3}$,
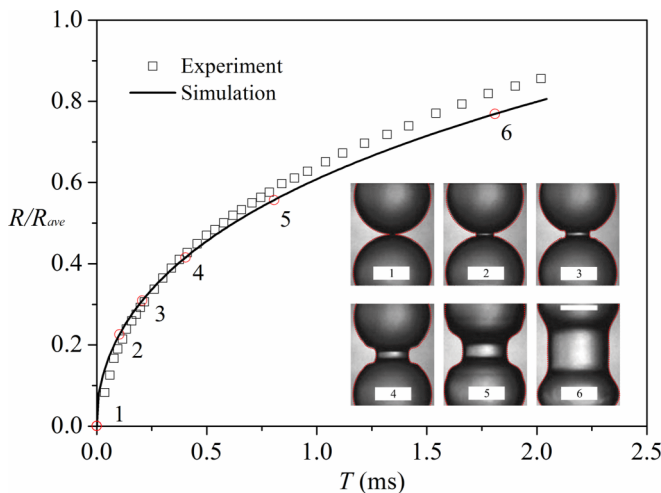
FIG. 4. Comparison of the droplet coalescence speed between experiment [29] and simulation. The controlling parameters are $\text{Oh} = 2.5 \times 10^{-3}$, $\Delta = 1.06$. The red-dotted lines in the sub-images are droplet interfaces obtained from the present simulation. Note that although $\Delta = 1.06$ was reported in the original work, $\Delta = 1.02$ was measured from the experimental images and therefore adopted in the simulation.

and $\mu_g/\mu_l = 1.83 \times 10^{-2}$. The six subimages illustrate the experimental evolution of the droplet interface, which is compared with the simulated interface in red dotted lines. It is seen that the simulation results well predict the coalescence process. Quantitative comparison of the coalescence speed is shown in the main plot of Fig. 4, where R is the radius of the expanding neck (or bridge) between the two droplets and R_{avg} is the average radius of the two droplets. Again, the simulation results are in good agreement with the experiment data. The slight deviation could be attributed to the original experimental setup, where each droplet was either pendent or sessile in gravitational environment, with their far ends being attached to a tube, so that the two droplets are not strictly spherical. Before we proceed, it is noted that Fig. 4 displays a scaling dependence of $R \sim \sqrt{t}$, with the scaling coefficient being approximately $1.1(\sigma R_{\text{avg}}/\rho_l)^{1/4}$. This is consistent with the scaling law for droplet coalescence dominated by inertia, which was proposed by Eggers *et al.* [27] and experimentally validated by Wu *et al.* [69] and Aarts *et al.* [30]. Thus, it justifies that the current droplet coalescence study belongs to the inertial regime.

IV. PHENOMENOLOGICAL DESCRIPTION OF INTERNAL JETLIKE MIXING

A. Representative case study

As a representative case, the coalescence of n-decane droplets was first investigated for a fixed Ohnesorge number of $\text{Oh} = 1.56 \times 10^{-2}$ and various size ratios. To show the long-time behavior of the internal mixing, the simulation lasts until $T = 4.0$. The small gas–liquid density ratio, $\rho_g/\rho_l = 1.68 \times 10^{-3}$, and the small gas–liquid viscosity ratio, $\mu_g/\mu_l = 1.96 \times 10^{-2}$, suggest that the gas inertia and viscosity are unlikely to cause any significant influence on the phenomena, as has been discussed in Sec. II. To facilitate our presentation, only three size ratios, namely, $\Delta = 1.8$, 2.2, and 2.8 are shown in Fig. 5(a). The mixing process is illustrated in the right half of each simulation image and the variation of local pressure, normalized by $3\sigma/D_S$, is shown in the left half image.

Phenomenologically, the entire process from the commencement of droplet coalescence to $T = 4.0$ can be divided into four stages according to the characteristics of droplet deformation and jet formation.

(1) *Stage I* (about $T = 0.00 \sim 0.20$): upon the droplet coalescence at the contact point, an interfacial ring cusp is formed in the vicinity of the point and tends to be smoothed out under the
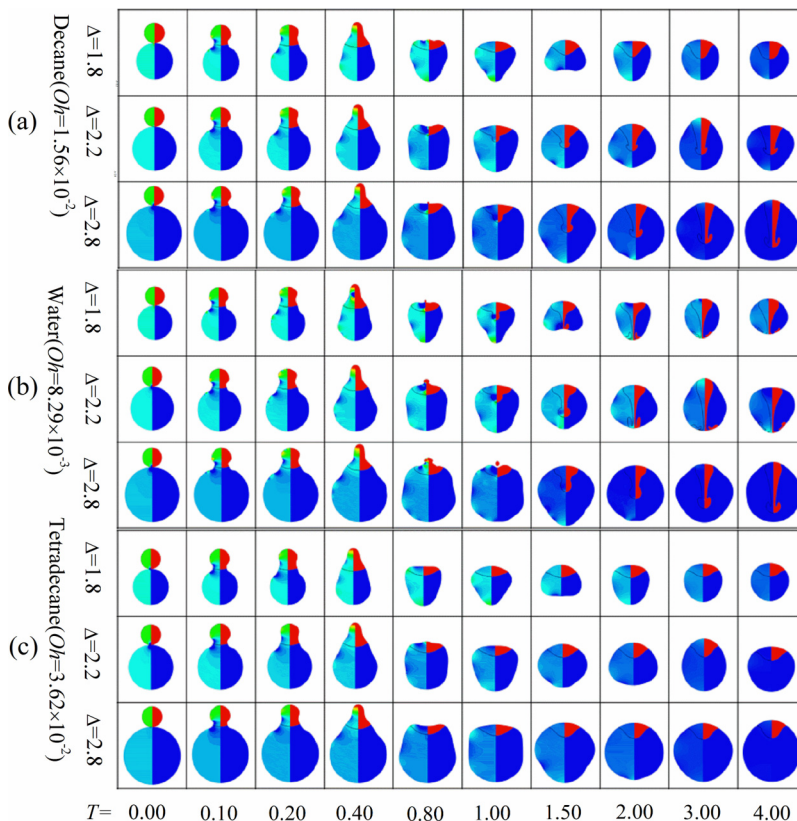
FIG. 5. Deformation and mixing upon the coalescence of initially stationary droplets of (a) n-decane with $t_c = 0.50$ ms, (b) water with $t_c = 0.33$ ms, and (c) n-tetradecane with $t_c = 0.48$ ms, and for different Δ ($\Delta = 1.8, 2.2, 2.8$). The left contour shows the static pressure, with the magnitude ranging from 0.0 of blue to 2.0 of red. The right contour plots the tracer variable, with red and blue tracking the fluid initially from the small and large droplets, respectively.

high capillary pressure. This causes a rapid, radially outward movement of the ring interface at the beginning stage of droplet coalescence. In the meantime, most of the mass in the droplets do not have noticeable movement along the axial direction. As a result, away from the vicinity of the ring cusp, the droplets remain almost spherical and the local pressures do not vary significantly.

(2) *Stage II* (about $T = 0.20 \sim 0.40$): the mass in the smaller droplet is driven into the larger one under the capillary pressure difference of about $4\sigma(D_S^{-1} - D_L^{-1})$. A finger-like bulge with a round head is consequently formed on the far side of the smaller droplet, as clearly seen at $T = 0.40$. The radius of the round head of the bulge, denoted by D_B, is smaller than that of the initial droplet, and thereby results in larger capillary pressure (shown in red) in the bulge than that in the large droplet.

(3) *Stage III* (about $T = 0.40 \sim 0.80$): the bulge merges into the droplet under the capillary pressure difference of about $4\sigma(D_B^{-1} - D_L^{-1})$. The mass of the bulge obtains an axial momentum in the vicinity of the axis as the result of the conversion of the surface energy of the bulge to its kinetic energy. After the bulge completely merges into the droplet, the pressure inside the droplet becomes almost uniform regardless of the slight local pressure variation due to the droplet oscillation.

(4) *Stage IV* (about $T = 0.80 \sim 4.00$): the final stage is characterized by the long-time behavior of the jetlike mixing, which is affected by the viscous dissipation of the internal flow motion and the droplet oscillation. It is seen that all the cases show jetlike mixing patterns except the case of

$\Delta = 1.8$, in which the merged smaller droplet lodges on the larger one to form a dome shape during the entire stage.

B. Influences of Oh and Δ

For a comparative study of the phenomena, the above simulations were repeated for water and n-tetradecane, which provide experimentally realizable comparison with n-decane for studying the influences of surface tension and viscosity. Specifically, the viscosity of water (8.9×10^{-4}Pa s) at room temperature is very close to that of n-decane (8.5×10^{-4}Pa s), but the surface tension of water (7.29×10^{-2}N/m) is almost three times larger than that of n-decane (2.38×10^{-2}N/m). The surface tension of n-tetradecane (2.65×10^{-2}N/m) is similar to that of n-decane, but its viscosity (2.03×10^{-3}Pa s) is substantially larger than that of n-decane. The simulation results for the coalescence of water droplets at various size ratios and with Oh $= 8.29 \times 10^{-3}$, $\rho_g/\rho_l = 1.22 \times 10^{-3}$, and $\mu_g/\mu_l = 1.80 \times 10^{-2}$, are shown in Fig. 5(b). The results for the coalescence of n-tetradecane droplets with Oh $= 3.62 \times 10^{-2}$, $\rho_g/\rho_l = 1.61 \times 10^{-3}$, and $\mu_g/\mu_l = 7.94 \times 10^{-3}$ are shown in Fig. 5(c). Again, the influence of gas inertia and viscosity can be neglected because of the small gas–liquid density and viscosity ratios. It is noted that Oh of n-tetradecane droplet almost doubles that of n-decane droplet, which in turn doubles that of water droplet. Several observations can be made by comparing the results shown in Fig. 5, as follows.

First, owing to the smaller Oh and thereby decreased viscous dissipation of water droplets, the mushroom-like jet emerges at $\Delta = 1.8$, as shown in Fig. 5(b), but it is absent for either n-decane or n-tetradecane droplets at the same size ratio, as shown in Figs. 5(a) and 5(c), respectively. It is also noted that the jetlike mixing pattern is absent for n-tetradecane droplets at all the size ratios. These results accord with and extend the earlier experimental observation of Anikumar et al. [46] that the formation of "mushroomlike" jet is suppressed by increasing the droplet viscosity.

Second, for the cases with the emergence of the distinct jetlike mixing, water droplets display enhanced and faster mixing compared with n-decane droplets, as shown in Fig. 5(b) compared with Fig. 5(a) for $\Delta = 2.2$. It is seen that the jet penetrates the whole droplet and hits the bottom surface at $T = 2.0$ for the water droplet, but the jet penetration is about a half of the droplet size for the n-decane droplet at the same time. In view of the characteristic time t_c of the water droplet is smaller than that of the n-decane droplet of the same size, the evolution of the jetlike mixing in the former is even faster and more substantial.

Third, an interesting albeit incidental phenomenon was observed for the water droplets of $\Delta = 2.8$, as shown in Fig. 5(b). A thin neck forms on the bulge and pinches off the bulge to generate a satellite droplet, which subsequently re-merges into the "father" droplet, as shown at $T = 1.00$. Although the jetlike mixing pattern still emerges, it is not as prominent as the case without the pinch-off. In the experimental study of the pinch-off phenomenon during the coalescence of unequal-size droplets, Zhang et al. [62] found that there exists a critical Δ_{cr} for the emergence of pinch-off and that Δ_{cr} increases monotonically with Oh. For Oh $= 8.29 \times 10^{-3}$, the predicted Δ_{cr} is about 2.6, which slightly overshoots 2.3 observed in Zhang et al.'s experiments. The overshooting is caused by that the increasingly attenuated liquid neck is not sufficiently resolved in the present study. Physically, pinch-off occurs when two interfaces become sufficiently close to one another, being of $O(10)$ nm, so that the van der Waals force triggers the interface collapse. Quantitatively predicting the pinch-off requires the numerical resolution of an extremely thin liquid neck, which is computationally challenging and therefore bypassed in the present study by limiting out scope to the size ratios below the critical ones determined by Zhang et al.'s experiment [62].

C. Regime nomogram of jetlike mixing

The above comparative study has suggested that Oh and Δ are crucial to the appearance of the internal mixing. To further quantify the influences of Oh and Δ on the formation of the jetlike mixing pattern, we extended the simulations to wider ranges of these two parameters. The resulting $\Delta - $ Oh
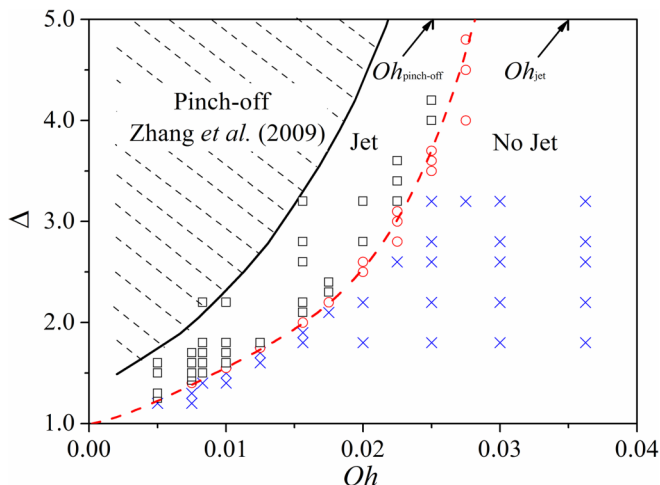
FIG. 6. Regime nomogram of initially stationary droplet coalescence in the $\Delta - $ Oh parametric space. The jetlike mixing is denoted by the square, the no-jet regime by the cross, and the transition by the circlet. The red-dashed fitting line is given by the fourth-order polynomial, $\Delta = 1.3691 \times 10^7 \, \mathrm{Oh}^4 - 4.6129 \times 10^5 \, \mathrm{Oh}^3 + 6.4108 \times 10^3 \, \mathrm{Oh}^2 + 25.0344 \, \mathrm{Oh} + 1$. The dashed area corresponds to the ranges of Δ and Oh effecting droplet pinch-off, experimentally given by Zhang *et al.* [62].

regime nomogram of the parametric study is shown in Fig. 6, where the open triangles denote the cases with distinct jetlike mixing and the open squares those without jetlike mixing.

For a given Oh, the jetlike mixing occurs as the size ratio is increased above a critical value indicated by the dashed line. Phenomenologically, the nondimensional capillary pressure difference, $4(1-\Delta^{-1})$, between the small and large droplets, increases with Δ and could be a driving force for the jet formation. Furthermore, Fig. 5 also shows that as increasing the size ratio the coalescence-induced internal flow tends to be concentrated around the symmetry axis, which could serve as an additional source promoting the jet formation. It can be also observed that the critical Δ for the emergence of the internal jet increases with Oh, which again verifies the observations from Fig. 5 that larger Oh tends to suppress the jet formation. At this point, considering the trend of the red-dashed curve in Fig. 6, one might be curious if there exists a threshold Oh beyond which jet formation is completely suppressed. Theoretically, this is highly possible since any jet is a convective phenomenon that could be inhibited by sufficiently large viscosity. Realizing that such a threshold can be determined numerically by simulating the case with near-infinity size ratio, which is computational challenging, we instead simulate the limiting problem: an inertialess droplet merged into a liquid pool. The result is marked by $\mathrm{Oh}_{\mathrm{jet}}$ in Fig. 6, which shows that the mushroomlike jet does not appear when Oh is increased above 0.035. The details about this simulation are not provided here for brevity.

For a complete phenomenological description of the problem, Zhang *et al.*'s experimental data on the emergence of droplet pinch-off are also plotted in Fig. 6 as a shadow regime. It is noted that pinch-off does not occur for Oh > 0.025 in their experiment.

V. MAIN VORTEX RING AND ITS ROLE IN INTERNAL JETLIKE MIXING

A. Identification of main vortex ring synchronized with internal jetlike mixing

We have demonstrated the dependence of the emergence of the internal jet on Oh and Δ, however the basic mechanism of the jet formation still requires further investigation. As has been discussed in the Introduction, the generation of the jetlike mixing pattern should not be fundamentally different from other similar jetting phenomena, for example a starting vortex jet [70–72] formed due to the self-induced motion of a single vortex ring. This conjecture is partly substantiated in Fig. 7 by the
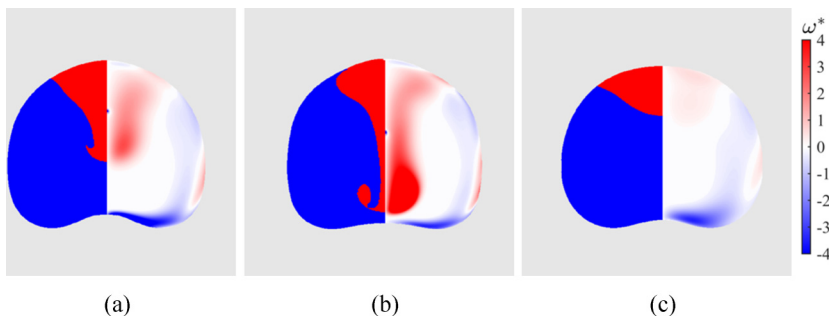
FIG. 7. Comparison between the tracer variable distribution (left) and vorticity contour (right) at $T = 1.70$ for the cases of (a) n-decane, (b) water, and (c) n-tetradecane with $\Delta = 2.2$. The color bar applies to the vorticity contours throughout the paper.

similar appearance of the jetlike structure and the vortex ring inside the merged droplet, characterized by normalized vorticity, $\omega^* = \omega t_c$. From previous studies [70–72], the formation of a starting jet can be boiled down to two essential problems: what is the source of vorticity forming the vortex ring? and how does the vortex ring detach from its source to form the jet? Similarly, we can illustrate the two important processes, namely, the generation of vorticity and the detachment of the main vortex ring, for the distinct internal jet subsequent to the droplet coalescence.

To study the generation and evolution of the main vortex ring that is responsible for the formation of the internal jet, one needs to first identify and track the region of the vortex. For the present problem having axisymmetry, we employ a simple vorticity-contour approach and consider the vorticity contour, $\omega = \omega_v$, encircling the main vortex as the vortex boundary, where ω_v is a small threshold vorticity. The results for a representative case (n-decane droplets with $\Delta = 2.2$) are presented in Fig. 8, where the green contour on the left side of the droplet represents the identified boundary of the main vortex. By comparing the green contour with the vorticity contour on the right side of the droplet, we indeed verify the vorticity-contour approach to be effective in capturing the main vortex among other vortices emerging at different stages of droplet coalescence.

The identification of the main vortex region also enables the estimation of the total vorticity within the main vortex. The total vorticity is evaluated by calculating the circulation

$$\Gamma_V = \int_{A_V} \omega dA$$

where A_V is the cross-section area of the main vortex. It should be noted that the volumetric integration over the volume, V_V, of the main vortex, $\int_{V_V} \omega dV$, is not an appropriate quantity for measuring the total vorticity. This is because Kelvin's circulation theorem [60,73] dictates that Γ_V is a conserved quantity in an ideal axisymmetric flow, but the volumetric integration is dependent on the radial distance of the vortex from the axis (Saffman [60], Eq. (1.5.22)). It is seen in Fig. 8 that Γ_V first increases and then decreases at a slower rate, implying the existence of two physical processes: vorticity generation and vortex detachment, that will be discussed in detail in Secs. V B and V C.

The calculation of the total vorticity provides further justification for the correlation between the main vortex ring and the internal jetlike mixing at different stages of droplet coalescence.

(1) *Stage I:* as the initial droplet coalescence occurs, it can be observed from Fig. 8(a) that vorticity develops only in the vicinity of the initial coalescence point, where surface deformation and its induced flow start. The rapid, outward expansion of the contacting region between the two droplets causes dramatic changes in the droplet geometry and velocity, thereby contributing to a fast rate of vorticity generation.

(2) *Stage II:* when the initial coalescence region has sufficiently expanded as shown in Fig. 8(b), the initial conversion from surface energy to kinetic energy gradually reaches stagnant. As a result, the velocity and the geometry of the droplet enter a slow-variation stage, causing a gradual vorticity
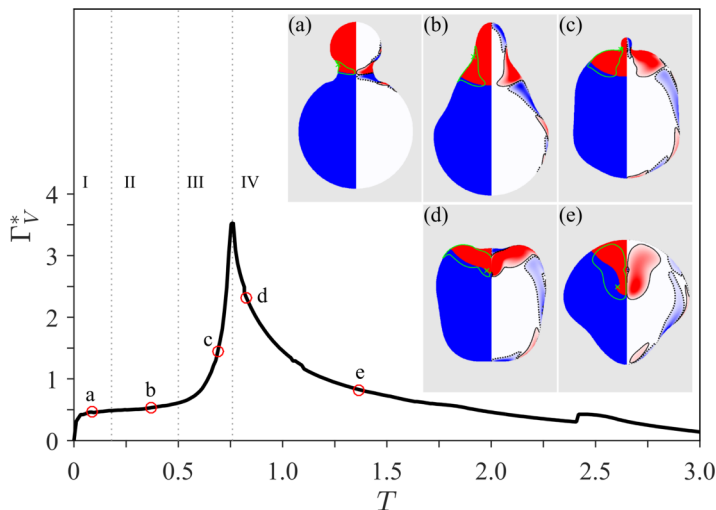
FIG. 8. The main plot shows the evolution of the nondimensional circulation of the main vortex for n-decane droplet coalescence with $\Delta = 2.2$, and Oh $= 1.56 \times 10^{-2}$. The subfigures (a)–(e) are the tracer variable plot (left) and vorticity contour (right) at the typical times (red circlets) on the vorticity evolution curve. In each subfigure, the green contour on the left side of the droplet represents the boundary of the main vortex identified through the vorticity-contour approach. The green cross marks the center of the main vortex corresponding to the local maximum vorticity. For clarity of illustration, positive and negative vortices in the vorticity contour are encircled by solid and dashed contour lines, respectively.

generation inside the main vortex. By the end of this stage, the remainder of the smaller droplet becomes an axial fingerlike liquid bulge, forming a new neck which would lead to the next peak of surface energy discharge.

(3) *Stage III:* the fluid bulge collapses into the large droplet under surface tension as shown in Fig. 8(c). Similar to Stage I, a substantial amount of surface energy of the merged interface is rapidly converted to the kinetic energy of the induced flow around the confined neck region of the small fluid bulge, resulting in massive vorticity production in the main vortex.

(4) *Stage IV:* after the complete merge of the fluid bulge into the large droplet, the main vortex ring starts to detach from the droplet surface and eventually forms the internal jet, as shown in Figs. 8(d) and 8(e). During this detaching process, the circulation of the main vortex ring first declines rapidly because of the diffusion of negative vorticity from the surface, and then drops gradually because of viscous dissipation after the complete detachment of the vortex ring.

B. Formation and growth of main vortex ring in stages I and III

In this section, we focus on the process of vorticity generation associated with the main vortex. As has been discussed in the Introduction, Batchelor [58] extended Helmholtz's third theorem [60] or Kelvin's circulation theorem [59,60] to the viscous flows, and summarized that "vorticity cannot be created or destroyed in the interior of a homogeneous fluid under normal conditions, and is produced only at boundaries" (p. 266 of Ref. [58]). Therefore, the initial generation of vorticity associated with the main vortex must happen at the gas–liquid interface. For the present problem, the significantly smaller density and viscosity of gas compared with those of liquid enable us to approximate the liquid-gas interface as a free surface with a vanishing shear stress [56,70,71] on it. In the reference frame defined in Fig. 1, the shear stress has the form

$$\sigma = \hat{\boldsymbol{n}} \cdot \nabla \boldsymbol{u} \cdot \hat{\boldsymbol{t}} + \hat{\boldsymbol{t}} \cdot \nabla \boldsymbol{u} \cdot \hat{\boldsymbol{n}} = 0, \tag{6}$$
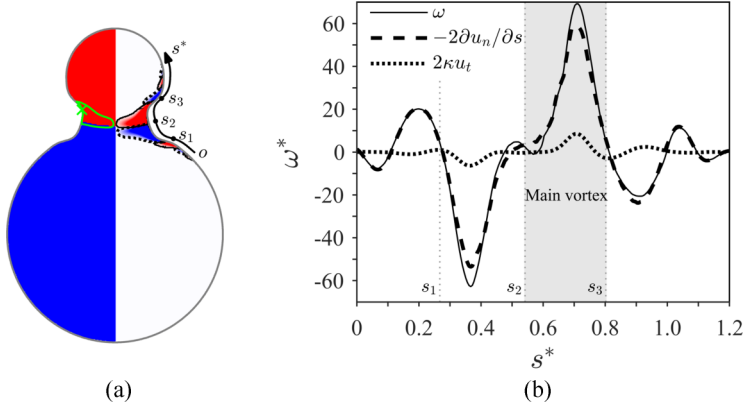
FIG. 9. (a) The tracer variable plot (left) and vorticity contour (right) at a representative instant of Stage I [Fig. 6(a)] for n-decane droplet coalescence with $\Delta = 2.2$, and Oh $= 1.56 \times 10^{-2}$. The green contour marks the boundary of the main vortex. (b) The vorticity distribution along the gas–liquid interface near the main vortex. The s^* coordinate is along the surface of the droplet, as indicated by the black arrow in (a).

and hence

$$\omega = \hat{\boldsymbol{n}} \cdot \nabla \boldsymbol{u} \cdot \hat{\boldsymbol{t}} - \hat{\boldsymbol{t}} \cdot \nabla \boldsymbol{u} \cdot \hat{\boldsymbol{n}} = -2\hat{\boldsymbol{t}} \cdot \nabla \boldsymbol{u} \cdot \hat{\boldsymbol{n}} \neq 0. \tag{7}$$

According to Lundgren and Koumoutsakos [57], the interface vorticity in Eq. (7) could be further decomposed into two parts by

$$\omega = -2\frac{\partial \boldsymbol{u}}{\partial s} \cdot \hat{\boldsymbol{n}} = -2\frac{\partial u_n}{\partial s} + 2\,\kappa u_t, \tag{8}$$

where $\kappa = \hat{\boldsymbol{t}} \cdot \partial \hat{\boldsymbol{n}}/\partial s$ is the local curvature of the surface; u_n and u_t are the velocity components normal and tangential to the surface, respectively. Equation (8) means that the only source of vorticity for the current problem is the interfacial flow and is affected by both the interface geometry and the interfacial flow velocities (gradients). For steady flows where the free surface is stationary, u_n becomes zero and the first term of Eq. (8) could be dropped out. For the present problem that is highly unsteady and involves significant deformation of the interface, both terms of Eq. (8) individually affects the vorticity generation of the main vortex at different stages. Furthermore, Eq. (8) can be interpreted that vorticity generation at a free surface is inevitable in the presence of either surface deformation or flow along curved surface. Due to the effect of viscosity, the vorticity generated at the interface would be diffused into the bulk fluid. In a low viscosity fluid, the diffusion mainly happens at a thin layer close to the interface, thus forming a surface-attached viscous shear layer or boundary layer, outside of which the flow is primarily convective. In this sense, the viscous shear layer should be considered more as an evidence of the diffusive vorticity transportation from the interface to the bulk fluid of low viscosity, rather than a source of vorticity itself.

Figure 9 shows the distribution of vorticity at the gas–liquid interface where massive vorticity is being generated initially inside the main vortex at Stage I. We can observe that a main peak of positive vorticity is located between s_2 and s_3, which corresponds to the portion of the interface overlapping with the boundary of the main vortex. This verifies that the growth of the total vorticity inside the main vortex shown in Fig. 8 is indeed related to the non-zero vorticity generation at the interface. Furthermore, the vorticity contributions from the two terms of Eq. (8) are also plotted in Fig. 9. It is seen that the first term, $-2\partial u_n/\partial s$, almost equals the vorticity itself, and the second term, $2\,\kappa u_t$, is negligible. This implies that the initial vortex generation in Stage I is mainly caused by the normal velocity gradient in the tangential direction of the outwardly moving surface, as the movement of surface is normal to the surface and u_n decreases from s_2 to s_3. It is interesting to note that vorticity generation is approximately symmetric with respect to the contacting plane of the two
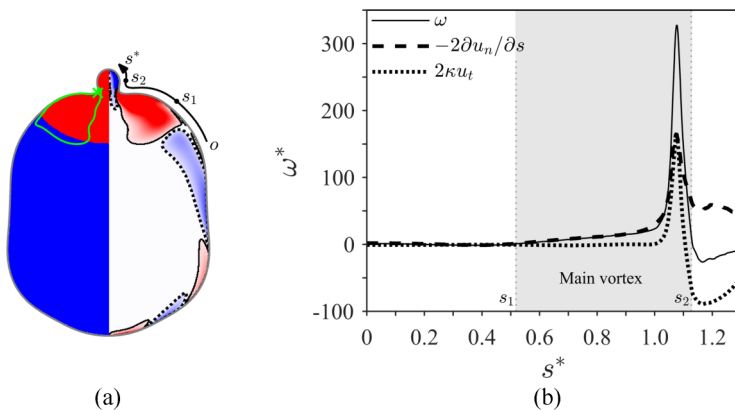
FIG. 10. (a) The tracer variable plot (left) and vorticity contour (right) for a representative instant of Stage III [Fig. 6(c)] for n-decane droplet coalescence with $\Delta = 2.2$ and Oh $= 1.56 \times 10^{-2}$. (b) The corresponding vorticity distribution along the gas–liquid interface near the main vortex.

droplets during Stage I. Specifically, a counterrotating vortex is created on the large droplet side from the surface between s_1 and s_2, with the $-2\partial u_n/\partial s$ term again dominating the vorticity generation. Although this "negative" vortex is only slightly weaker than the main vortex, it gradually decays in later stages, whereas the main vortex will be further enhanced.

In Sec. V A, we have seen that Stage III corresponds to the primary vorticity generation phase for the main vortex. To understand the underlying mechanism of vortex growth during this stage, Fig. 10 plots the vorticity distribution along the gas–liquid interface at the instant corresponding to Fig. 8(c). Here, the curve between s_1 and s_2 represents the portion of the gas–fluid interface associated with the main vortex. It can be observed that major vorticity generation occurs in the vicinity of the connecting point between the bulge and the main droplet. The two vorticity components in Eq. (8) are also plotted in Fig. 10, and their peaks are comparable to each other along the interface of the main vortex. This indicates that both the interface deformation and the large curvature equally contribute to the significant vorticity generation during this stage. It is also noted that, in the region beyond the main vortex and toward the axis, the tangential velocity and curvature combined generate negative vorticity, which exceeds the positive vorticity generated by interface deformation, causing the emergence of a negative vortex inside the small bulge.

C. Detachment of main vortex ring in stage IV

The above analysis answers the question about where the vorticity inside the internal jet comes from, but it does not explain how the concentrated vorticity becomes a self-induced vortex ring that subsequently translates within the droplet to form an internal jet. In other words, the cumulation of vorticity inside a vortex ring does not guarantee the formation of a jet. Taking the starting jet problem as an example, the jet formation criterion requires that the nondimensional formation time is larger than a certain value [71] (a typical number is 4), when the vortex ring is strong enough to "rip-off" its own vorticity-feeding shear layer; otherwise, the vorticity would keep growing inside the vortex ring without detachment and thereby no jet can be formed.

For the formation of the internal jet due to droplet coalescence, we hypothesize that a similar mechanism exists such that the internal jet does not form until the main vortex ring detaches from the surface of the droplet. Consequently, there must be an additional mechanism that "peels" the original vortex ring off the surface. This problem resembles that of flow separation on a smooth body, where vorticity inside the boundary layer detaches from the surface to become a free vortex in the wake. It is well-known that flow separation happens where the adverse pressure gradient is strong enough to generate vorticity opposite to the original shear layer. Analogically, we hypothesize that the
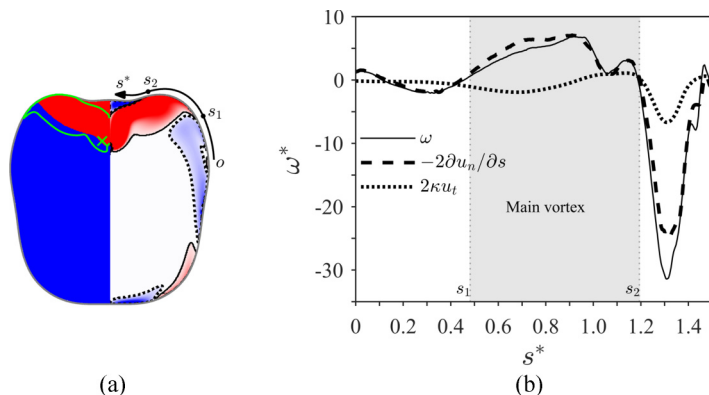
FIG. 11. (a) The tracer variable plot (left) and vorticity contour (right) for a representative instant of Stage IV [Fig. 6(d)] for n-decane droplet coalescence with $\Delta = 2.2$ and Oh $= 1.56 \times 10^{-2}$. (b) The corresponding vorticity distribution along the gas–liquid interface near the main vortex.

emergence of negative vorticity at the liquid-gas interface would be responsible for the detachment of the main vortex ring.

To verify this hypothesis, we plot the vorticity distribution along the surface of the droplet at the beginning of Stage IV, as shown in Fig. 11. It is confirmed that the main vortex starts to detach from the central portion of the interface ($s^* > s_2$) where significant negative vorticity is generated. Moreover, Fig. 11 also shows that the negative vorticity generation near the axis is largely attributed to the first term of Eq. (8), $-2\partial u_n / \partial s$. We further recognize that this negative vorticity generation actually corresponds to an outward retraction of the dented surface subsequent to the complete merge of the droplet. In analogy to flow separation, s_2 can be considered as a dynamic flow separation point, which moves in the radial direction as the negative vortex region expands out, and cut off the main vortex from the surface in a razorlike fashion. After the main vortex completely detaches from the surface, it becomes a free vortex ring translating with its self-induced velocity to form an internal jet.

Here, the new information obtained in this section is emphasized. Ever since the phenomenon of the jetlike mixing following droplet coalescence was reported by Anilkumar *et al.* [46], researchers have been curious about its formation mechanism. Nobari and Tryggvason [47] calculated the evolutions of the surface and kinetic energies, and attributed the formation of the internal jet to a rapid release of surface energy during the injection of the small drop. This explanation is further substantiated by Liu *et al.*'s recent work [48]. We noted that, while this "surface energy" theory covers the fundamentals of the jet formation, it does not give the whole picture to the phenomenon as sufficient details about the process are still lacking. Specifically, from the vortex dynamics perspective, two conditions are necessary for a vortex ring to evolve into a jet: the accumulation of vorticity and the separation from the vorticity source. Through the current analysis, we managed to trace the origination of the main vortex ring back to the initial coalescence stage. Furthermore, we found that the vortex ring grows substantially due to a combined effect of dramatical interface deformation and large interface curvature during the entry of the small droplet, which coincides with the period of rapid surface energy discharge found by Nobari and Tryggvason [47]. Finally, after the entry of the small droplet a reverse motion of the interface induces a negative shear layer, which facilitates the detachment of the main vortex ring from the liquid-gas and consequently initiates the formation of the internal jet.

VI. VORTEX-RING-CRITERION FOR INTERNAL JET FORMATION

Previous sections have demonstrated that the emergence of the internal jet after droplet coalescence is closely related to the generation and detachment of the main vortex. In this section, we shall seek quantitative criterion of the internal jet based on the main vortex ring.
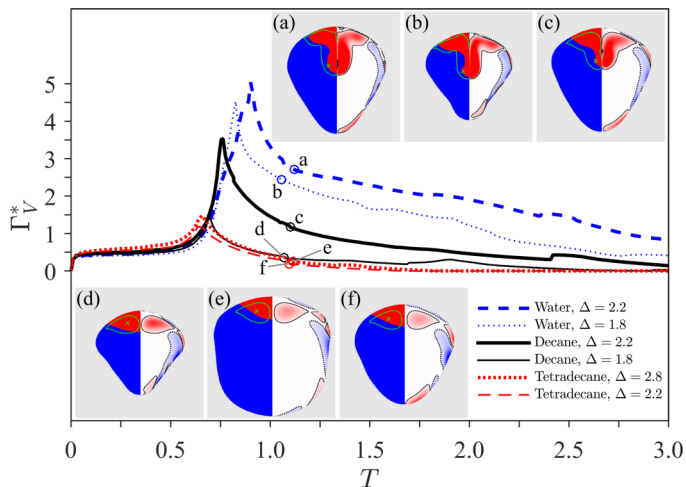
FIG. 12. Evolution of the nondimensional circulation around the main vortex for different cases of droplet coalescence. The subfigures (a)–(f) present the tracer variable plot (left) and vorticity contour (right) for the instants when the main vortex completely detaches from the surface of the droplet. The circulations corresponding to these instants are also marked on the evolution curves.

We start by comparing the evolution of the main vortex between cases with the internal jet (water droplets with $\Delta = 1.8$, 2.2 and n-decane droplets with $\Delta = 2.2$) and those without the internal jet (n-decane droplets with $\Delta = 1.8$ and n-tetradecane droplets with $\Delta = 1.8$, 2.2), as shown in Fig. 12. The droplet configurations and vorticity contours at the instant when the vortex ring completely detaches from the droplet surface are also presented in the figure, with their corresponding total vorticities being marked on the circulation evolution curves, respectively. It is seen that, at the instant of vortex detachment, the cases without jet formation have significantly lower total vorticity compared with the cases with jet formation. Moreover, the lower circulation for the cases without jet formation should be attributed to either shorter period or smaller rate of vorticity generation during Stage III. It is noted that the less total vorticity generated during Stage III is related to the diminished bulge structure created at the end of Stage II, which does not possess enough surface energy to be converted during Stage III.

The above analysis qualitatively indicates that the internal jet appears only if the vortex ring is strong enough by the end of the vortex detachment. Physically, an ideal free vortex ring would readily translate downstream and form a jet under its self-induced flow, unless the viscosity significantly dissipates the vortex ring. Consequently, the formation of the internal jet after the vortex detachment is determined by the competition between the advective momentum associated with the vortex ring and the momentum lost due to viscous diffusion. To characterize this competition, a Reynolds number can be defined by

$$\mathrm{Re}_J = \frac{U_V r_V}{\nu}, \tag{9}$$

where U_V and r_V are the characteristic translational velocity and the radius of the free vortex ring, respectively. Based on the dynamics of a vortex ring [60], U_V can be expressed as

$$U_V = \frac{\Gamma_V}{4\pi r_V}. \tag{10}$$

Combining Eqs. (9) and (10) gives

$$\mathrm{Re}_J = \frac{\Gamma_{VD}}{4\pi \nu} = \frac{\Gamma_{VD}^*}{4\pi \mathrm{Oh}}, \tag{11}$$
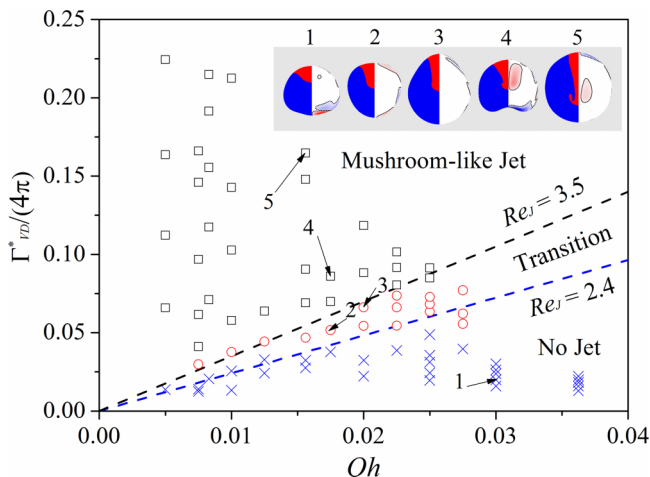
FIG. 13. Validation of the vortex criterion for the jet formation for different cases of droplet coalescence. The slopes of the two dashed lines correspond to $\text{Re}_J = 2.4$ and $\text{Re}_J = 3.5$, marking the transition from the no-jet regime to the mushroom-like jet regime. Here, all data points correspond to the cases of different Δ and Oh plotted in Fig. 6.

where Γ_{VD} (and its nondimensional form Γ_{VD}^*) represents the circulation of the main vortex ring when it completely detaches from the droplet surface.

With Γ_{VD}^* calculated in a similar approach to Fig. 12 (circulations associated with the circlets), Eq. (11) can be validated for different cases of droplet coalescence, as shown in the $\text{Oh} - \Gamma_{VD}^*$ regime nomogram in Fig. 13. The mushroomlike jet formation occurs with about $\text{Re}_J > 3.5$, no jet formation with $\text{Re}_J < 2.4$, and in-between is a transition regime. The transition from the "no-jet" regime to the "mushroom-like jet" regime with increasing Re_J is manifested by the five typical cases from 1 to 5, as shown in the subfigures of Fig. 13. Thus, the jet number Re_J serves as a phenomenological criterion for jet formation subsequent to the coalescence of two initially stationary droplets. It is noted that the data points presented in Fig. 13 were calculated from their corresponding simulation cases in Fig. 6. While Fig. 6 introduces the phenomenological observation of the dependence of the internal jet on the initial conditions (Δ and Oh), Fig. 13 provides the fundamental mechanism explaining how the internal jet forms. Last, we emphasize that this jet-formation criterion does not depend on any presumption or initial condition of the merging droplets, indicating a prospect of extending this criterion to determining internal jet formation in more general situations, such as droplet collision and other microfluidic interactions.

VII. CORRELATION BETWEEN VORTEX-INDUCED JET AND INTERNAL MIXING

As discussed in the Introduction, the present work was motivated to understand the influence of the jetlike structure on internal mixing. It is noted that the word "mixing" is used to describe the mass transfer between two droplets. In general, the mass transfer is twofold, namely, convective and diffusive. In the current study, the mass diffusion is neglected for two reasons. One is that the two droplets contain the same type of fluid, thus the concept of "mass diffusion" does not apply as there is no species concentration gradient. Second, even if two miscible fluids are considered, the Peclet number, which can be defined by $\text{Pe} = \sqrt{\sigma D_S/\rho_l}/D_m$, where D_m is the mass diffusivity, is estimated to be greater than $O(10^2)$ for the current problem, meaning that the effect of convection significantly overweighs the mass diffusion. Therefore, mixing in this study primarily reflect the effect of mass convection.
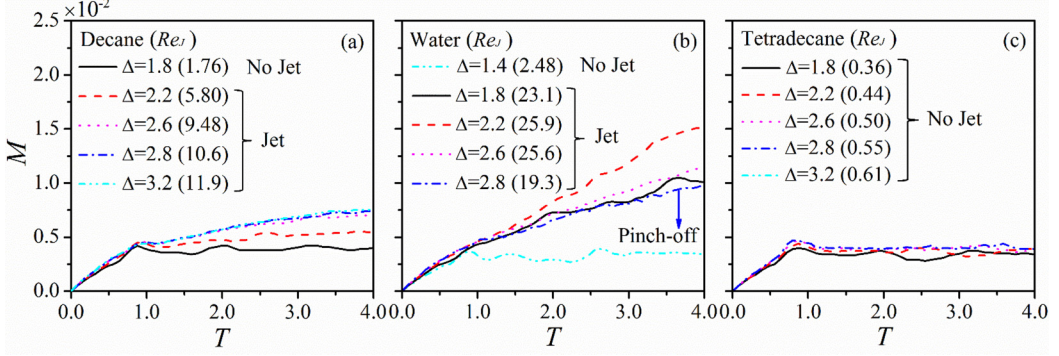
FIG. 14. Time evolution of the mixing index for n-decane ($Oh = 1.56 \times 10^{-2}$), water ($Oh = 8.29 \times 10^{-3}$), and n-tetradecane ($Oh = 3.62 \times 10^{-2}$) droplets of various size ratios. Re_J for each case is presented in the parentheses to relate the performance of mixing to the formation of internal jet.

The comparative study in Sec. IV has qualitatively demonstrated that mixing between the two droplets is intimately related to the mushroomlike jet. Specifically, the occurrence of the jet seems to cause large stretching and roll-up of the interfaces of two droplets, thereby increasing the contacting surface and contributing to enhanced mixing performance. To further quantify this observation on the internal mixing within the merged droplet, a mixing index M independent of Oh and Δ can be defined as follows [10,74]:

$$M = 1 - \frac{\int_V |C - C_\infty| H(f - 1) dV}{\int_V |C_0 - C_\infty| H(f - 1) dV}, \tag{12}$$

where the VOF function $f = 0$ in the gas and $f = 1$ in the droplets; the Heaviside step function $H(f - 1)$ limits the integration domain to be within the droplets. C, C_0, and C_∞ are the distribution functions of the time-dependent "concentration" of the small droplet liquid in the merged mass, in the unmixed droplets, and in the fully mixed mass, respectively, and are defined by

$$C = |2\phi - 1| C_0, \quad C_0 = \begin{Bmatrix} 0, & \phi = 0 \\ 1, & \phi > 0 \end{Bmatrix}, \quad C_\infty = 1/(1 + \Delta^3), \tag{13}$$

where ϕ is the spatially and temporally varying dye function, which is defined as 1 in the small droplet and 0 in the large droplet. Therefore, M varies between 0 and 1 with larger value indicating better mixing.

The time evolution of the calculated M for n-decane, water, and n-tetradecane and for various Δ are shown in Fig. 14. The slope of the curves quantifies the rate of mixing at different times. Several observations can be made about the mixing processes.

First, for all the cases, the mixing rate seems to be independent of Oh or Δ at Stages I-III (up to around $T = 0.8$), when the small droplet has not completely merged into the larger one. This is because mixing in the early stages are mostly caused by the geometrical changes of the two-droplet configuration. These changes are associated with the coalescence of interfaces around the initial contacting point (Stage I), the expansion of the contacting surface (Stage II), and the collapse of the liquid bulge (Stage III), which to a considerable extent are similar processes among cases with different Oh or Δ.

Second, the increase of M during Stage IV substantially varies with Oh and Δ, suggesting the important role of the jetlike structure that does not present until this stage. The values of Re_J for different cases are presented in the parentheses to indicate the correlation between jet formation and internal mixing. It is seen that, for small Re_J cases where no internal jet is formed, the average mixing rate is approximately zero in Stage IV and is almost independent of Re_J. Together with the above-discussed mixing independency during Stages I–III, it seems that mixing is intrinsically

self-similar throughout the merging process if no internal jet presents. This, in turn, provides a direct evidence that the vortex-induced jet has a significant impact on the internal mixing of the merged droplet.

Third, for those cases where mushroomlike jet forms, Re_J measures the relative strength of the vortex ring associated with the internal jet. Therefore, larger Re_J corresponds to a stronger jet, and in turn indicates larger convective momentum or lower viscous dissipation or both; enhanced mixing rate is consequently expected. This can be readily verified by the n-decane cases shown in Fig. 14(a), where the average mixing rate seems to monotonically increase with Re_J. Furthermore, comparing the n-decane cases with the water cases shown in Fig. 14(b), we can also confirm that the water cases in general has larger mixing rates than the n-decane cases, as the water cases have larger Re_J.

Fourth, it is noted that the monotonic dependence of the mixing rate on Re_J seems to not hold exactly for the water cases. Specifically, the $\Delta = 2.2$ case has much larger mixing rate than the $\Delta = 2.6$ case, although Re_J for the two cases are nearly the same. This can be attributed to the tendency of droplet pinch-off for the water case with $\Delta = 2.6$, where the surface energy responsible for the interface oscillations at the later stage of internal mixing is significantly reduced. Moreover, for the cases with droplet pinch-off, the long-term mixing performance is also affected by the surface oscillations after the jet has penetrated through the merged droplet and hit the gas–liquid interface on the opposite side.

Finally, for the cases with internal jet but without droplet pinch-off, the average mixing rate also monotonically increases with Δ or decreases with Oh, which is consistent with our observation from Fig. 5 that the jetlike mixing becomes more prominent with increasing Δ or decreasing Oh. It should be mentioned that the penetration depth of the fluid from the small drop was analyzed by Nobari and Tryggvason [47] to provide an indicator for the mixing effect, which is reasonable considering that the penetration depth is closely related to the strength of the internal jet. Thus, their results also show a similar monotonicity of the penetration depth with Δ for small Oh cases where internal jet exists. However, they did not quantify the mixing preformation for the internal jets, which have penetrated through the large drop and hit the surface of the other side. In this sense, the mixing index M of the current study is an improved approach in quantifying the mixing performance of droplet coalescence.

VIII. CONCLUDING REMARKS

In this paper, the coalescence of two initially stationary droplets of unequal sizes was investigated numerically using an improved VOF method and adaptive mesh refinement algorithm, with emphasis on two key problems: the formation of the internal jet and its effect on mixing between the two droplets.

Phenomenologically, the jetlike mixing was perceived based on three representative fluids, water, n-decane, and n-tetradecane. It was found that both decreasing the fluid viscosity and increasing the size ratio would facilitate the emergence of the jetlike mixing. This observation was further justified by a regime nomogram describing the occurrence of the jetlike mixing with varying size ratio and Ohnesorge number.

The fundamental mechanism responsible for forming the internal jet was understood by first identifying the correlation between the jetlike structure and the main vortex ring inside the merged droplet. Based on the evolution of the main vortex ring, we identified three stages crucial to the jet formation, namely, vortex-ring formation, vortex-ring growth, and vortex-ring detachment. The initial vortex generation upon droplet coalescence, albeit being small in magnitude, is mainly caused by the normal velocity gradient in the tangential direction of the outwardly merging surface around the coalescence point. The rapid collapse of the small bulge into the large droplet, which results in dramatic interface deformation and local large-curvature interface, causes massive vorticity generation and therefore vortex-ring growth. The outward retraction of the dented surface promotes the generation of negative vorticity that detaches the main vortex ring from the surface to form a self-induced jet.

Furthermore, an analysis concerning the circulation of the main vortex ring was performed by comparing cases with and without the internal jet. The result points to a positive correlation between the occurrence of the internal jet and the circulation of the main vortex ring after its complete detachment. Recognizing that the formation of the internal jet is the outcome of a competition between the convective momentum carried with the vortex ring and the viscous dissipation, we defined a special Reynolds number, Re_J, as the criterion for jet formation. It was verified through various droplet coalescence cases that $Re_J > 3.5$ approximately gives the mushroom-like jet and $Re_J < 2.4$ predicts no jet formation, with in-between marking the transition regime.

A mixing index was defined to quantify the effect of the internal jet on mixing. For the cases without internal jet formation, the average mixing rate has a minor dependence on Δ or Oh, reflecting an intrinsic self-similarity associated with the configuration evolution of the two-droplet system during their coalescence. For the cases with internal jet formation, the average mixing rates are however significantly enhanced and the mixing index tends to monotonically increase with increasing Δ or decreasing Oh.

Because Re_J physically characterizes the relative strength of the detached vortex ring, which controls the strength of the forming jet, we compared Re_J among cases of different Δ or Oh to seek a direct correlation between the vortex-induced jet and internal mixing. It was confirmed that the average mixing rate of the vortex-ring detachment stage grows monotonically with Re_J for large Re_J cases with jet formation. It should be noted that the above observations and conclusions only hold for the cases without droplet pinch-off or the tendency of pinch-off, because pinch-off will dramatically reduce the surface energy driving the interface oscillation, which affects the mixing in the jet-formation stage.

---

[1] M. Gorokhovski and M. Herrmann, Modeling primary atomization, Annu. Rev. Fluid Mech. **40**, 343 (2008).

[2] H. P. Kavehpour, Coalescence of drops, Annu. Rev. Fluid Mech. **47**, 245 (2015).

[3] J. P. Reid and L. Mitchem, Laser probing of single-aerosol droplet dynamics, Annu. Rev. Phys. Chem. **57**, 245 (2006).

[4] A. L. Yarin, Drop impact dynamics: Splashing, spreading, receding, bouncing . . . , Annu. Rev. Fluid Mech. **38**, 159 (2006).

[5] R.-H. Chen, Diesel–diesel and diesel–ethanol drop collisions, Appl. Therm. Eng. **27**, 604 (2007).

[6] H.-H. Chiu, Advances and challenges in droplet and spray combustion. I. Toward a unified theory of droplet aerothermochemistry, Prog. Energy Combust. Sci. **26**, 381 (2000).

[7] P. Jenny, D. Roekaerts, and N. Beishuizen, Modeling of turbulent dilute spray combustion, Prog. Energy Combust. Sci. **38**, 846 (2012).

[8] S. K. Aggarwal, Single droplet ignition: Theoretical analyses and experimental findings, Prog. Energy Combust. Sci. **45**, 79 (2014).

[9] Z. Liu, J. Wu, H. Zhen, and X. Hu, Numerical simulation on head-on binary collision of gel propellant droplets, Energies **6**, 204 (2013).

[10] C. Tang, J. Zhao, P. Zhang, C. K. Law, and Z. Huang, Dynamics of internal jets in the merging of two droplets of unequal sizes, J. Fluid Mech. **795**, 671 (2016).

[11] Y. J. Jiang, A. Umemura, and C. K. Law, An experimental investigation on the collision behavior of hydrocarbon droplets, J. Fluid Mech. **234**, 171 (1992).

[12] T. B. Low and R. List, Collision coalescence and breakup of raindrops. Part II: Parameterization of fragment size distribution Fragmentation, J. Atmos. Sci. **39**, 1607 (1982).

[13] T. B. Low and R. List, Collision, coalescence and breakup of raindrops. Part I: Experimentally established coalescence efficiencies and fragment size distributions in breakup, J. Atmos. Sci. **39**, 1591 (1982).

[14] N. Ashgriz and J. Y. Poo, Coalescence and separation in binary collisions of liquid drops, J. Fluid Mech. **221**, 183 (1990).

[15] J. Qian and C. K. Law, Regimes of coalescence and separation in droplet collision, J. Fluid Mech. **331**, 59 (1997).

[16] K.-L. Pan, P.-C. Chou, and Y.-J. Tseng, Binary droplet collision at high Weber number, Phys. Rev. E **80**, 036301 (2009).

[17] C. Rabe, J. Malet, and F. Feuillebois, Experimental investigation of water droplet binary collisions and description of outcomes with a symmetric Weber number, Phys. Fluids **22**, 047101 (2010).

[18] G. Brenn, D. Valkovska, and K. D. Danov, The formation of satellite droplets by unstable binary drop collisions, Phys. Fluids **13**, 2463 (2001).

[19] G. Brenn and V. Kolobaric, Satellite droplet formation by unstable binary drop collisions, Phys. Fluids **18**, 087101 (2006).

[20] G. Brenn, in *Handbook of Atomization and Sprays*, edited by N. Ashgriz (Springer, Berlin, 2011).

[21] K. D. Willis and M. E. Orme, Experiments on the dynamics of droplet collisions in a vacuum, Exp. Fluids **29**, 347 (2000).

[22] K. D. Willis and M. E. Orme, Binary droplet collisions in a vacuum environment: An experimental investigation of the role of viscosity, Exp. Fluids **34**, 28 (2003).

[23] K.-L. Pan, C. K. Law, and B. Zhou, Experimental and mechanistic description of merging and bouncing in head-on binary droplet collision, J. Appl. Phys. **103**, 064901 (2008).

[24] F. Y. Testik, A. P. Barros, and L. F. Bliven, Toward a physical characterization of raindrop collision outcome regimes, J. Atmos. Sci. **68**, 1097 (2011).

[25] J.-P. Estrade, H. Carentz, G. Lavergne, and Y. Biscos, Experimental investigation of dynamic binary collision of ethanol droplets—a model for droplet coalescence and bouncing, Int. J. Heat Fluid Flow **20**, 486 (1999).

[26] C. Tang, P. Zhang, and C. K. Law, Bouncing, coalescence, and separation in head-on collision of unequal-size droplets, Phys. Fluids **24**, 022101 (2012).

[27] J. Eggers, J. R. Lister, and H. A. Stone, Coalescence of liquid drops, J. Fluid Mech. **401**, 293 (1999).

[28] L. Duchemin, J. Eggers, and C. Josserand, Inviscid coalescence of drops, J. Fluid Mech. **487**, 167 (2003).

[29] S. T. Thoroddsen, K. Takehara, and T. G. Etoh, The coalescence speed of a pendent and a sessile drop, J. Fluid Mech. **527**, 85 (2005).

[30] D. G. Aarts, H. N. Lekkerkerker, H. Guo, G. H. Wegdam, and D. Bonn, Hydrodynamics of Droplet Coalescence, Phys. Rev. Lett. **95**, 164503 (2005).

[31] Y. Pan and K. Suga, Numerical simulation of binary liquid droplet collision, Phys. Fluids **17**, 082105 (2005).

[32] C. Focke and D. Bothe, Direct numerical simulation of binary off-center collisions of shear thinning droplets at high Weber numbers, Phys. Fluids **24**, 073105 (2012).

[33] X. Chen and V. Yang, Thickness-based adaptive mesh refinement methods for multi-phase flow simulations with thin regions, J. Comput. Phys. **269**, 22 (2014).

[34] R. W. Hopper, Coalescence of two viscous cylinders by capillarity: Part I, Theory, J. Am. Ceram. Soc. **76**, 2947 (1993).

[35] R. W. Hopper, Coalescence of two viscous cylinders by capillarity: Part II, Shape evolution, J. Am. Ceram. Soc. **76**, 2953 (1993).

[36] G. A. L. van de Vorst, Integral method for a two-dimensional Stokes flow with shrinking holes applied to viscous sintering, J. Fluid Mech. **257**, 667 (1993).

[37] G. A. L. van de Vorst, *Modelling and numerical simulation of viscous sintering* (Technische Universiteit Eindhoven, Eindhoven, Netherlands, 1994).

[38] R. Narhe, D. Beysens, and V. S. Nikolayev, Contact line dynamics in drop coalescence and spreading, Langmuir **20**, 1213 (2004).

[39] W. D. Ristenpart, P. M. McCalla, R. V. Roy, and H. A. Stone, Coalescence of Spreading Droplets on a Wettable Substrate, Phys. Rev. Lett. **97**, 064501 (2006).

[40] J. B. Boreyko and C.-H. Chen, Self-Propelled Dropwise Condensate on Superhydrophobic Surfaces, Phys. Rev. Lett. **103**, 184501 (2009).

[41] M. W. Lee, D. K. Kang, S. S. Yoon, and A. L. Yarin, Coalescence of two drops on partially wettable substrates, Langmuir **28**, 3791 (2012).

[42] F. Liu, G. Ghigliotti, J. J. Feng, and C.-H. Chen, Numerical simulations of self-propelled jumping upon drop coalescence on non-wetting surfaces, J. Fluid Mech. **752**, 39 (2014).

[43] H. Minemawari, T. Yamada, H. Matsui, J. y. Tsutsumi, S. Haas, R. Chiba, R. Kumai, and T. Hasegawa, Inkjet printing of single-crystal films, Nature **475**, 364 (2011).

[44] A. M. Nightingale, T. W. Phillips, J. H. Bannock, and J. C. de Mello, Controlled multistep synthesis in a three-phase droplet reactor, Nat. Commun. **5**, 3777 (2014).

[45] F. Blanchette, Simulation of Mixing Within Drops Due to Surface Tension Variations, Phys. Rev. Lett. **105**, 074501 (2010).

[46] A. V. Anilkumar, C. P. Lee, and T. G. Wang, Surface-tension-induced mixing following coalescence of initially stationary drops, Phys. Fluids A **3**, 2587 (1991).

[47] M. R. Nobari and G. Tryggvason, The flow induced by the coalescence of two initially stationary drops, NASA Technical Memorandum 106752 (1994).

[48] D. Liu, P. Zhang, C. K. Law, and Y. Guo, Collision dynamics and mixing of unequal-size droplets, Int. J. Heat Mass Transfer **57**, 421 (2013).

[49] F. Blanchette, L. Messio, and J. W. M. Bush, The influence of surface tension gradients on drop coalescence, Phys. Fluids **21**, 072107 (2009).

[50] J. Castrejón-Pita, K. Kubiak, A. Castrejón-Pita, M. Wilson, and I. Hutchings, Mixing and internal dynamics of droplets impacting and coalescing on a solid surface, Phys. Rev. E **88**, 023023 (2013).

[51] K. Sun, M. Jia, and T. Wang, Numerical investigation on the head-on collision between unequal-sized droplets with multiple-relaxation-time lattice Boltzmann model, Int. J. Heat Mass Transfer **70**, 629 (2014).

[52] K. Sun, T. Wang, P. Zhang, and C. K. Law, Non-Newtonian flow effects on the coalescence and mixing of initially stationary droplets of shear-thinning fluids, Phys. Rev. E **91**, 023009 (2015).

[53] R. W. Cresswell and B. R. Morton, Drop-formed vortex rings—The generation of vorticity, Phys. Fluids **7**, 1363 (1995).

[54] G. Agbaglah, M.-J. Thoraval, S. T. Thoroddsen, L. V. Zhang, K. Fezzaa, and R. D. Deegan, Drop impact into a deep pool: vortex shedding and jet formation, J. Fluid Mech. **764**, R1 (2015).

[55] M.-J. Thoraval, Y. Li, and S. T. Thoroddsen, Vortex-ring-induced large bubble entrainment during drop impact, Phys. Rev. E **93**, 033128 (2016).

[56] B. S. Dooley, A. E. Warncke, M. Gharib, and G. Tryggvason, Vortex ring generation due to the coalescence of a water drop at a free surface, Exp. Fluids **22**, 369 (1997).

[57] T. Lundgren and P. Koumoutsakos, On the generation of vorticity at a free surface, J. Fluid Mech. **382**, 351 (1999).

[58] G. K. Batchelor, *An Introduction to Fluid Dynamics* (Cambridge University Press, Cambridge, UK, 1967).

[59] P. K. Kundu and I. M. Cohen, *Fluid Mechanics* (Academic Press, Cambridge, 2010).

[60] P. G. Saffman, *Vortex Dynamics* (Cambridge University Press, Cambridge, 1992).

[61] P. Zhang and C. K. Law, An analysis of head-on droplet collision with large deformation in gaseous medium, Phys. Fluids **23**, 042102 (2011).

[62] F. H. Zhang, E. Q. Li, and S. T. Thoroddsen, Satellite Formation During Coalescence of Unequal Size Drops, Phys. Rev. Lett. **102**, 104502 (2009).

[63] R. Scardovelli and S. Zaleski, Direct numerical simulation of free-surface and interfacial flow, Annu. Rev. Fluid Mech. **31**, 567 (1999).

[64] G. Tryggvason, A. Esmaeeli, J. Lu, and S. Biswas, Direct numerical simulations of gas/liquid multiphase flows, Fluid Dyn. Res. **38**, 660 (2006).

[65] S. Popinet, Gerris: A tree-based adaptive solver for the incompressible Euler equations in complex geometries, J. Comput. Phys. **190**, 572 (2003).

[66] S. Popinet, An accurate adaptive solver for surface-tension-driven interfacial flows, J. Comput. Phys. **228**, 5838 (2009).

[67] X. Chen and V. Yang, Effect of ambient pressure on liquid swirl injector flow dynamics, Phys. Fluids **26**, 102104 (2014).

[68] J. C. Cano-Lozano, R. Bolaños-Jiménez, C. Gutiérrez-Montes, and C. Martínez-Bazán, The use of Volume of Fluid technique to analyze multiphase flows: Specific case of bubble rising in still liquids, Appl. Math. Model. **39**, 3290 (2015).

[69] M. Wu, T. Cubaud, and C.-M. Ho, Scaling law in liquid drop coalescence driven by surface tension, Phys. Fluids **16**, L51 (2004).

[70] N. Didden, On the formation of vortex rings: Rolling-up and production of circulation, Zeitschrift für Angewandte Mathematik und Physik (ZAMP) **30**, 101 (1979).

[71] M. Gharib, E. Rambod, and K. Shariff, A universal time scale for vortex ring formation, J. Fluid Mech. **360**, 121 (1998).

[72] M. Shusser and M. Gharib, Energy and velocity of a forming vortex ring, Phys. Fluids **12**, 618 (2000).

[73] K. Mohseni, H. Ran, and T. Colonius, Numerical experiments on vortex ring formation, J. Fluid Mech. **430**, 267 (2001).

[74] S.-I. Yeh, W.-F. Fang, H.-J. Sheen, and J.-T. Yang, Droplets coalescence and mixing with identical and distinct surface tension on a wettability gradient surface, Microfluid. Nanofluid. **14**, 785 (2013).